Compositional Fluctuations Mediated by Excess of Tellurium in Bismuth Antimony Telluride Nanocomposite Yields High Thermoelectric Performance

Nagendra S. Chauhan,[1,2]* Sergey V. Pyrlin,[3] Oleg I. Lebedev,[4] Luis S. A. Marques,[3] Marta M. D. Ramos,[3] Tanmoy Maiti,[2] Kirill Kovnir,[5,6] Brian A. Korgel,[7] and Yury V. Kolen'ko[1]*

[1]*International Iberian Nanotechnology Laboratory (INL), Braga 4715-330, Portugal*
[2]*Plasmonics and Perovskites Laboratory, Indian Institute of Technology, Kanpur, Uttar Pradesh 208016, India*
[3]*Centro de Física das Universidades do Minho e do Porto, Universidade do Minho, 4710-057, Braga, Portugal*
[4]*Laboratoire CRISMAT, UMR 6508, CNRS-Ensicaen, Caen 14050, France*
[5]*Department of Chemistry, Iowa State University, Ames, Iowa 50011, USA*
[6]*Ames Laboratory, U.S. Department of Energy, Ames, Iowa 50011, USA*
[7]*McKetta Department of Chemical Engineering, The University of Texas at Austin, Austin, Texas 78712, USA*

Abstract

The high thermoelectric figure of merit (*ZT*) in state-of-the-art bismuth antimony telluride (BST) composite was attained by excess tellurium-assisted liquid phase compaction approach. Herein, we report a maximum $ZT \approx 1.4$ at 500 K attained for BST bulk nanocomposite fabricated by spark plasma sintering of colloidally-synthesized $(Bi, Sb)_2Te_3$ platelets and Te-rich rods. The Te-rich nanodomains and antimony-precipitation during sintering results in compositional fluctuations and atomic ordering within BST–Te eutectic microstructure, which provides additional phonon scattering and hole contributions. The electrical transport measurement and theoretical calculations corroborate the altered free carrier density via. lattice defects and atomic ordering in Te-rich conditions, resulting in higher power factor. Microstructural studies suggest that reduction in lattice thermal conductivity is due to composite interfaces and defects in closely packed $(Bi, Sb)_2Te_3$ matrix with unevenly distributed Sb and Te rich nanodomains. This work provides an unconventional chemical synthesis route with large scalability for developing high-performance chalcogenides-based bulk nanocomposites for TE applications.

Keywords: *Thermoelectric; Chalcogenides, Colloidal Synthesis; Spark Plasma Sintering; Transport Property; Microstructure*

*Corresponding author: nagendra599@gmail.com; yury.kolenko@inl.int
Tel.: +351 253 140 112 (Ext. 2534); Fax (351) 253 140 119

1. INTRODUCTION

The solid-state thermoelectric (TE) transport phenomena involve direct inter-conversion between heat and electricity, which is actively studied nowadays for applications involving waste heat recovery, remote power supplies, portable device cooling, *etc.* Such TE based energy conversion devices operates either in power generation mode due to Seebeck effect, or in refrigeration mode via Peltier effect. However, in both these modes, efficiency of energy conversion is determined using the same dimensionless TE figure of merit (ZT), which is conventionally expressed as $ZT = \left(\frac{S^2\sigma}{\kappa}\right)T$; where S, σ, and κ represents the Seebeck coefficient, electrical conductivity, and thermal conductivity at the absolute temperature (T).[1, 2] To maximize the TE energy conversion efficiency, higher ZT and larger temperature differential (ΔT) between the hot and cold sides is needed. However, owing to intrinsic difficulties in decoupling electrons and phonons in bulk solids for ZT enhancement, the TE conversion efficiency of bulk materials continues to remain low, when compared with the other existing waste heat recovery technologies, such as organic rankine cycles, recuperators, regenerators, *etc.*[3] Nevertheless, TE offers a promising prospect for power generation from heat with $ZT > 1$ materials in near room temperature regime, wherein bismuth antimony telluride and its derivatives have remained the state-of-the-art TE material and has been extensively used for cooling application in most successfully commercialized Peltier refrigerators.[2, 4]

It is now recognised that $(Bi, Sb)_2Te_3$ solid solutions exhibit the highest ZT among any of the existing material in near room temperature regime due to their relatively high carrier mobility, μ, and lower lattice thermal conductivity, κ_L. Despite the possibility of alloying, Bi_2Te_3–Sb_2Te_3 system as *p*-type or *n*-type materials, these alloys are widely recognised as excellent *p*-type material with $Bi_{0.5}Sb_{1.5}Te_3$ as the most optimised composition[4]. To further enhance the ZT of these optimally alloyed composition, doping with Cu,[5, 6] Cd,[7] Ag,[8, 9] Pb[10]

and nanostructuring via ball milling,[5, 6, 9, 11, 12] melt-spinning,[13-15] and chemical synthesis[16, 17] were extensively carried out. Similarly, composite aspects of hybridization with nanoparticles such as Sb_2O_3,[18] SiC,[19] ZnO,[20] Zn_4Sb_3,[21] PbSe,[22] Y_2O_3,[23] and SiO_2[24] were demonstrated for tuning the TE transport favorably.

Lately, unconventional nanocomposite approaches with Te-excess composition[14, 16] were found to be most effective in attaining higher *ZT* in contrast to earlier conviction[25] that "*ZT* of a macro-composite cannot exceed the largest value of its constituents under most practical conditions". For instance, ultralow κ due to dense dislocation arrays embedded in grain boundaries by liquid-phase compaction of $Bi_{0.5}Sb_{1.5}Te_3$ bulks, resulted in $ZT \approx 1.86$ at 320 K[14]. Similarly, formation of crystallographically textured nanomaterials by solution re-precipitation mechanism led to an unprecedented $ZT \approx 1.96$ at 420 K[16]. Thus, nanocomposite strategies have been highly effective in p-type $(Bi, Sb)_2Te_3$ based TE materials for attaining optimal phonon and electron transport properties within and beyond the alloy limit.

Recently, we established a convenient colloidal synthesis of complex metal chalcogenides nanoparticles (NPs) [26-28]. In this work, we broaden the scope of our scalable colloidal synthesis to attain colloidal Bi–Sb–Te nanoplatelets and Te-rich nanorods. These nanoparticles were subsequently consolidated employing spark plasma sintering into bulk nanocomposite exhibiting a maximum $ZT \approx 1.4$ at higher temperature of 500 K as compared to state-of-the-art BST alloys. The microstructural changes during sintering were found to be accompanied by telluride-spilling and antimony *in situ* precipitation as secondary phases, which resulted in compositional fluctuations and atomic ordering within Bi–Sb–Te matrix, thereby providing additional phonon scattering with minimal effect on carrier scattering and mobility. The detailed structural characterization and transport properties measurement were correlated and TEs performance of the bulk nanocomposites were understood using theoretical inputs for low temperature TE based power generation applications.

2. RESULTS

2.1 Nanoparticles synthesis and fabrication of bulk BST nanocomposite. The selected composition was determined based on high *ZT* attained in optimal $Bi_{0.5}Sb_{1.5}Te_3$,[4, 11, 14] while the synthesis procedure (see *Supplementary Information* sections S1–3 for details) and reaction conditions were guided by our recently developed colloidal synthesis route for chemical synthesis of complex metal chalcogenides NPs.[27] An excess of 10 mol% of Ph_2Te_2 were used for the reaction with $Bi(ac)_3$ and $Sb(ac)_3$ in hexadecylamine (HDA) to account for the volatile nature and high vapour pressure of Te[16] and keeping in mind high *ZT* attained in Te-excess compositions.[14, 16] The Rietveld refinement of XRD pattern of the synthesized end-product is shown in Fig. 1a, which corresponds to a mixture of phases identified as $BiSbTe_3$, Bi_4Te_3, and Te. The refined parameters of these structurally similar phases are presented in Table S1. The measured peaks can be well indexed to the listed in Table S1 phases. corresponding to NPs, which belongs the rhombohedral crystal system, space group: $R\bar{3}$m (no. 166). The peaks corresponding to hexagonal Te phase, space group: $P3_121$ (no. 152), was also indexed suggesting its uniform presence within the synthesize nanoparticles mixture. The HDA based chemical synthesis route was initially employed to synthesize NPs on gram scale and were subsequently scaled up. The yield of the as-synthesized mixed phase Bi–Sb–Te NPs for each batch was estimated to be ca. 90% (≈ 4.5 g) from the presented colloidal chemistry approach.

The resultant Bi–Sb–Te nanopowder was subsequently consolidated into BST bulk nanocomposite by sintering at rapid heating rates employing spark plasma sintering (SPS). The Rietveld refined XRD patterns of the sintered BST pellets as shown in Fig. 1b, are well indexed with the corresponding phases observed in its NPs building blocks with additional peaks corresponding to Sb. Post SPS, the appearance of Sb peaks are in compliant with the previous observation of current-induced grain-boundary modification and Sb

nanoprecipitation in electrically sintered BST due to passage of high-density pulsed current ($\approx 10^3$ A cm^{-2}).[29]

The sintering profile for bulk BST nanocomposite synthesis (Fig. 2) comprises three steps wherein temperature and pressure are raised simultaneously. The average ramp rate for heating and cooling were ca. 40 K min^{-1} and 100 K min^{-1}. The maximum temperature of ≈700 K at which samples were sintered, is close to the melting point of the Te-rich eutectic, suggesting the possibility of Te-spilling due to liquid phase sintering. However, the absence of isothermal sintering at maximum temperature prevents Te spilling with lesser sample-to-sample variation with better processing and stoichiometric control. The synthesized NPs were loaded into a graphite die of diameter 12.7 mm and sintered at 700 K with pressure ≈ 50 MPa under vacuum ≈ 4–6 Pa for the compaction of nanopowder into denser BST pellets. The density of the SPS-sintered bulk Bi–Sb–Te nanocomposites obtained as pellets with dimension Ø12.7 mm × 2 mm was measured using the Archimedes principle (822 e Mettler Toledo) and were found to be ≈ 6.5 ± 0.2 g cm^{-3}.

2.2 Microstructural characterization reveals eutectic microstructure with antisite defects. A detailed microstructure studies by SEM and TEM imaging on the mixed phase Bi–Sb–Te NPs are shown in Fig 3. The SEM image (Fig. 3a) revealed homogeneous sub-micron size distribution of Bi–Sb–Te particles with nano-plates having thickness range of about a few tens of nano-meters. Also, particles with nanorod morphology having broad size distribution were simultaneously present along with nanoplatelets throughout the sample. The HAADF–STEM observation at low-magnification of the nanosized feature with plate (Fig. 3b) and rod (Fig. 3c) morphology and their respective STEM–EDX mappings revealed homogeneous distribution of the Bi, Sb, and Te elements in those particle appearances. Remarkably, particles with nanorods morphology displays Te rich chemical composition as confirmed by EDX analysis. To elucidate the structural arrangement in Bi–Sb–Te particles

synthesized by colloidal synthesis, we further conducted HAADF–STEM study in conjunction with SAED analysis (Fig. 3d). The representative high-resolution HAADF–STEM images of the as-synthesized plate-like particle along [100] zone axes, together with the respective SAED patterns displayed in Fig. 3e indicates highly crystalline and remarkably defect free sample.

The microstructural characterization of representative SPS-sintered bulk BST nanocomposite sample is shown in Figure 4, which reveals a eutectic type of microstructure. At lower magnification, a well-distributed darker region within brighter appearing matrix were evidenced in both secondary electron (SE) and back scattered electron (BSE) images, shown in Figs. 4a and 4b, respectively. However, the elemental mapping of corresponding region indicates uniform distribution of constituent element. The EDX analysis of matrix indicates varying atomic % of $Bi_xSb_{2-x}Te_3$ where x varies throughout the matrix, having an average chemical composition of $BiSbTe_3$ indicated for the brighter regions. This observed compositional fluctuation in brighter regions can be understood by examining the well distributed darker region at higher magnification for chemical composition.

The darker regions (Fig. 4a) probed at higher magnification, correspond to two phases, both of which are shown by SE images (Figs. 4d,4g), BSE image (Figs. 4e,4h), elemental mapping (Figs. 4f,4i) and EDS analysis, respectively. The dark region 1 indicates Te rich sites corresponding to Te nanorods (Fig. 4a), while the dark region 2 are sites where antimony precipitation was prevalent. The observed microstructural change and atomic ordering in SPS-sintered BST sample with Sb precipitation of secondary phases suggest current-induced electromigration of constituent elements due to thermal activation during sintering in bulk nanocomposite.[29] The presence of well distributed Te and Sb precipitates within the BST matrix having varied atomic ratio of Bi/Sb are favourable for enhancing phonon scattering. Despite, Te vaporization being prevalent at higher sintering temperature ≈ 700 K, the absence of Te-spilling results in eutectic type microstructure with decreased

interface density. The Te rich conditions and sintering near eutectic temperature results in BST–Te eutectic microstructure (Figs. 4a–4c), with Sb precipitation (Figs. 4g–4i) to form Sb_{Te} antisite defects (Figs. 4d–4f). The uniformly distributed secondary phases within SPS-consolidated BST matrix and their implication on the electrical and thermal transport properties of BST nanocomposite is further analysed by theoretical predictions and transport properties measurement.

2.3 BST with high power factor and low thermal conductivity. The Bi–Sb–Te based compounds belong to class of a layered semiconductors with anisotropic TE properties, due to its anisotropic transport properties, which originates from the intrinsically misfit layered crystal structures.[30, 31] The electrical transport properties, i.e., σ and S were experimentally measured along both in-plane and cross-plane direction. For theoretical comparison and understanding, the thermoelectric coefficients were estimated along the axis of the hexagonal unit cell (*c*-axis) and perpendicular to it (along the *ab* plane). This is also because in case of $(Bi,Sb)_2Te_3$-based materials, the directions of the high charge mobility also correspond to the plane of easy cleavage of the crystal. Therefore, the *c*-axis of $(Bi,Sb)_2Te_3$ lattice is mostly oriented along the short side of the plate-like nanoparticles, which in turn is most likely oriented along cross-plane direction of the nanocomposite BST sample.

The electrical transport parameters σ and S are shown in Figs. 5a and 5b, which indicates *p*-type electrical conductivity with degenerate semiconducting behaviour, in the measured temperature regime. A higher value of σ was observed along both in-plane ($\sigma_{\text{in-plane}}$) and cross-plane ($\sigma_{\text{cross-plane}}$) direction, which is comparable to previously reported σ for BST compounds.[31, 32] The $\sigma_{\text{in-plane}}$ was found to be significantly higher than $\sigma_{\text{cross-plane}}$ as estimated theoretically, in line with previous experimental observation,[32, 33] which can be ascribed to crystallographic anisotropy in bismuth antimony telluride-based compounds.

To further understand the electrical transport room temperature hall measurement was carried out along cross-plane direction. The carrier mobility $\mu \approx 115 \pm 5$ cm^2 V^{-1} sec^{-1} and

carrier concentration $n \approx 8.2 \pm 0.5 \times 10^{19}$ cm^{-3} was measured for the representative specimens, suggesting both higher n and lower μ for the synthesized BST nanocomposite, when compared with previous report[34] on BST nanograined bulk material ($n \approx 2.5 \times 10^{19}$ cm^{-3}; $\mu \approx 264$ cm^2 V^{-1} sec^{-1}) and BST bulk ingot ($n \approx 1.8 \times 10^{19}$ cm^{-3}; $\mu \approx 298$ cm^2 V^{-1} sec^{-1}). The higher carrier concentrations can be ascribed to defect chemistry in the synthesized BST primarily due to Sb_{Te} antisite defects (Fig. 3c). The self-doping by antisite defects tends to control the intrinsic charge carrier concentration and determine the conduction type.[30] In the synthesized isoelectronic alloyed BST under Te-rich conditions, by taking into consideration the higher proportion of Sb_2Te_3 over Bi_2Te_3 and a comparatively lower formation energy of electron acceptor (Sb_{Te}) antisite defects over electron donor (Te_{Sb} and Te_{Bi}) defects, BST remains *p*-type in Te-rich conditions. The presence of Sb_{Te} antisite defects within the eutectic microstructure tends to enhance the n remarkably, resulting in higher σ and correspondingly lower Seebeck coefficient near room temperature in comparison to previous report on *p*-type BST alloys.[11, 14, 32]

The measured thermopower (Seebeck coefficient, S) is substantially higher than theoretical estimates, and exhibit relatively lesser influence than its counterpart σ for anisotropy. The suppressed bipolar conduction and shifting of thermal excitation of minority charge carriers to higher temperature were observed for S along both in-plane ($S_{\text{in-plane}}$) and cross-plane ($S_{\text{cross-plane}}$) direction, with a maximum value around 500 K. As observed, $S_{\text{cross-plane}}$ is relatively higher than $S_{\text{in-plane}}$ in the entire measurement range. The cumulative indicator of electrical charge transport, i.e., power factor ($PF = S^2\sigma$) is shown in Fig. 5c. The PF increases with increasing temperature up to 450 K and decreases thereafter to reach a maximum $PF_{\text{in-plane}} \approx 4 \times 10^{-3}$ W m^{-1} K^{-2} and $PF_{\text{cross-plane}} \approx 3 \times 10^{-3}$ W m^{-1} K^{-2}, respectively. A higher PF was observed along in-plane direction mainly because of higher $\sigma_{\text{in-plane}} >> \sigma_{\text{cross-plane}}$.

The electronic thermal conductivity, κ_e, as shown in Fig. 5d can be experimentally evaluated according to Wiedemann–Franz law $\kappa_e = L \times \sigma \times T$, where L is the Seebeck-dependent Lorenz number.[35] The L values are shown in the Supplementary Information Fig. S4, are in the range of (1.85–1.70) × 10^{-8} W Ω K^{-2}. Likewise theoretical estimates, the experimental κ_e varies marginally in the measured temperature range and is higher along in-plane direction, which is mainly due to higher $\sigma_{\text{in-plane}} >> \sigma_{\text{cross-plane}}$. The evolution of specific heat capacity (C_p) with temperature is shown in the Supplementary Information Fig. S5. The temperature-dependent C_p measurement of the synthesized nanostructured BST sample is higher and in closer proximity to the Dulong–Petit limit. Due to disk shaped sample requirement, the thermal diffusivity measurement was conducted only along cross-plane direction for two set of specimens prepared under similar sintering conditions.

The total thermal conductivity, κ, along cross-plane (Fig. 5e), was calculated using the equation $\kappa = D \times \rho \times C_P$. A drastic reduction in κ is observed mainly due to the nanoscale microstructural features (Fig. 4) resulting from Te-nanodomains and Sb-precipitates within the BST–Te eutectic microstructure, which specifically targets the scattering of low frequency phonons with long mean free path. The lattice thermal conductivity, κ_L, is calculated using the equation $\kappa_L = \kappa - \kappa_e$ and is presented along with κ in Fig. 5e. As seen from Figs. 5e and 5d, both κ_L and κ_e had substantial contribution to the κ. While κ_e is mostly a direct outcome of σ and cannot be reduced further, a significant reduction in κ_L was observed. Although quantitatively identifying different contributions of the nanostructures (such as Te-nanodomains and Sb-precipitates) to the transport properties is complicated, their presence tends to scatter all phonons with mean free paths in all-scale ranging from the micron scale down to the atomic scale, thus drastically reducing the thermal conductivity.

2.4 BST exhibiting $ZT_{max} \approx 1.4$ at around 500 K. Notably, both electrical and thermal transport measurement along the cross-plane direction for the thermally stabilised sample is

analysed for estimation of *ZT*, to marginalise the effect of non-homogeneity and crystallographic orientations introduced during sintering, thereby minimizing possibility of erroneous data. The temperature dependent *ZT* for the *p*-type BST nanocomposite prepared by colloidal synthesis followed by SPS sintering is shown in Fig. 5f. A maximum $ZT_{max} \approx 1.4$ at 500 K was attained due to the dramatically reduced κ with an enhanced *PF*. The synthesized BST nanocomposite display suppressed bipolar conduction and enhanced phonon scattering at the interfaces. The characteristically low κ_L attained in BST was mainly attributed to the enhanced scattering of phonons by arrays of dislocations at semi-coherent grain boundaries, nano-domains, and distortions in the lattice structure (Fig. 4). Such eutectic microstructure selective scatters phonons, while remaining ineffective scatterer for electrons/holes which have relatively longer wavelength, thus retaining a higher *n*, σ and *PF*. A drastic reduction in κ_L with a synergistic enhancement in *PF*, cumulatively results in a higher *ZT*.

From application perspective in case of high temperature sources, it is recognized that Bi_2Te_3-based materials can be segmented at low temperature ends, as they are best available TE materials in lower temperatures.[4] The concept of segmentation for increasing the TE efficiency requires difference in TE compatibility factor, *CF*, for the two TE materials should be less than a factor of 2. The *CF* was estimated using $CF = \frac{\sqrt{1+ZT}-1}{\alpha T}$,[36] and is shown in Fig. 3f. *CF* decreases with increasing temperature as a result of its direct correlation with ZT. This is comparable to the other state-of-the-art *p*-type available in mid-temperature regimes.[37] Thus, prepared *p*-type nanocomposites will be a suitable TE material for segmentation with high temperature mid-temperature TE materials for achieving highly efficient TE based power generation.

3. DISCUSSION

3.1 Correlation of phase constitutions with high TE performance. The phase constitution and synthesis methodology determine the physical and transport properties of a material. Bi–Sb–Te alloys are traditional *p*-type material widely used for fabricating commercialised Peltier devices operating near ambient temperature. The preparation of the bulk nanostructured high-performing material is often challenging, mainly due to the volatile nature and high vapour pressure of Te.[16] The Bi–Sb–Te phase diagram also indicates structural similar competing phases, such as $BiSbTe_3$, Sb_2Te_3, BiTe, Bi_3Te_4, with close formation energies.[30, 38] In this study, bulk nanocomposite for power generation applications is prepared from mixed phase nanoparticles synthesized by colloidal route followed by high temperature (≈ 700 K) SPS sintering to attain densified samples with eutectic type microstructure and prevalent Sb_{Te} antisite defects.

The idea of making composites with balanced material properties has long been exploited in materials research. Interestingly, it has been previously observed that excess of Te in $(Bi, Sb)_2Te_3$ compositions results in highly textured nanomaterials.[14, 16] We intended to design BST bulk nanocomposites for power generation application at above room temperature (≈ 500 K). For this purpose, we first prepared nanoparticle building blocks using colloidal synthesis. Previously, we have demonstrated this facile route for synthesizing high purity chalcogenide nanoparticles with controlled stoichiometry in low dimensions. [26-28] The structural characterisation of the as-synthesized nanopowder revealed co-existence of three phases. Specifically, two plate-like-shaped $(Bi, Sb)_2Te_3$ and Bi_4Te_3 structurally similar compounds (layered structures with hexagonal symmetry and larger *c*-axis lattice constants) are formed during colloidal synthesis, together with one rod-like-shaped Te phase corresponding to the excess of Te taken during colloidal synthesis. These mixed phase nanoparticles were then used as building blocks for bottom-up fabrication of nanostructured bulk BST material employing spark plasma sintering. The uniaxial pressure and sintering near eutectic temperature of BST assist the favorable microstructural changes forming Te-

rich nanodomains and Sb-rich precipitation within the eutectic microstructure of the resultant BST nanocomposite. While Te phase corresponding to Te rich nanorods within the synthesized nanoparticles promotes Sb_{Te} antisite defects resulting in higher *n*, σ and *PF*, the presence of Te-nanodomains and Sb precipitates led to significant lowering in κ_L. A maximum $ZT \approx 1.4$ at 500 K of BST nanocomposite prepared by novel colloidal synthesis followed by SPS consolidation is comparable to state-of-the-art *p*-type bismuth antimony telluride-based alloys. In particular, Fig. 6 shows a comparison of the synthesized BST nanocomposite with previously reported bulk nanostructured $(Bi,Sb)_2Te_3$ prepared by different methodologies, such as mechanical alloying,[5,11,12] melt spinning,[14,15] hydrothermal,[17] chemical synthesis,[16] along with state-of-the-art ingot,[11]. High achieved *ZT* emphasizes the prospect of reported material for waste heat recovery in low temperature regimes TE devices.

3.2 Comparison of Theoretical Calculations and Experimental Measurements: Despite the availability of wide range of studies on BTS system, the comparison of transport characteristics between the bulk crystalline material and nanostructured samples requires complex considerations. The hole concentration of *p*-type $(Bi, Sb)_2Te_3$ alloys can be altered by adjusting the Bi/Sb ratio or by preparation of materials in different thermodynamic states (e.g., Bi/Sb-rich, or Te-rich conditions). This is primarily due to occurrence of substantial doping in Bi_2Te_3-based materials via lattice defects, which alters the free carrier density and therefore the transport properties in a wider range.[30, 39-41] The relatively smaller difference in electronegativity and atomic sizes of Sb–Te in comparison with Bi–Te in the synthesized BST, induces antisite defects whose concentrations depends majorly upon the stoichiometric composition, temperature, and processing conditions at which the material was synthesized.

In nanostructured material, higher concentration of defects exists especially at nanoparticle interfaces.[42-44] Therefore, it is more insightful to compare experimental measurements with the theoretically calculated properties, estimated at the value of chemical potential yielding the same free carrier concentration as measured experimentally. For this

purpose, we compared the measured TE properties with the theoretical predictions from Boltzmann transport theory and DFT calculated band structure for $BiSbTe_3$ crystal. To acknowledge the effect of additional doping from defects and phase interfaces, the value of chemical potential for calculation of transport coefficients was chosen to reproduce the experimentally measured charge carrier density.

It is evident from the Fig. 5 that the experimental cross-plane and in-plane electrical transport are best described by the components of the thermoelectric coefficients along the hexagonal unit cell (*c*-axis) and perpendicular to it (along the *ab* plane). It was interesting to observe that while the measured σ and κ_e agree well with theoretical predictions, the measured thermopower (Seebeck coefficient) was substantially higher, than theoretical estimates. This is an interesting observation as it displays that the prepared nanocomposite sustains bulk-like electric conductivity, while suppressing lattice thermal conduction. The noticeable deviation of thermopower can be interpreted to be an effect of additional interfaces between semiconducting and metallic phases.[45]

3.3 Low temperature TE based power generators by suppressed bipolar conduction. Commercial TE technology at near room temperature was predominantly led by Bi_2Te_3 based Peltier cooling materials. Alongside, harvesting low-grade waste heat available in low temperature regimes is an active area of research particularly for rapidly growing wearable electronics markets. In this context, TE based power generators can be reliably employed for recovery of low temperature waste heat having low quality and low energy density. The TE performance of Bi_2Te_3 which is largely reported as a pseudo binary phase of Bi_2Te_3 and Sb_2Te_3 is majorly impeded by minority carrier excitation across the small bandgap even at room temperature, thus larger bandgap is needed for higher temperature operation where high thermal gradient is available. The semiconducting band gap[46] using the temperature (T_{max}) at which the thermopower (S) peaks, $E_g = 2e|S_{max}|T_{max}$ was roughly estimated to be

≈ 0.19 eV, which is narrow band gap in between the band of binary compound Bi_2Te_3 (0.13 eV) and Sb_2Te_3 (0.28 eV).[47] The modification of the crystalline structure and electronic density of states in the synthesized bulk nanocomposite by Te-rich nanodomains and Sb precipitation is found to be effective in inhibiting the onset of intrinsic conduction for suppressed bipolar diffusion. The average $ZT_{avg} \approx 1.1$ was observed in the range of 300–500 K, indicating a wider prospect of the synthesized BST nanocomposite for application in low-temperature TE power generation.

4. CONCLUSION

A facile and scalable colloidal synthesis successfully afforded a mixed phase nanopowder with plate- and rod-like morphologies of the constituent nanoparticles. The as synthesized nanopowder was subsequently consolidated at rapid heating rates employing SPS. The resultant bulk BST nanocomposite demonstrates average *ZT* value of 1.1 in the 300–550 K temperature regime. The observed remarkable TE performance is associated with high *n* and reduced κ_L due to BST–Te eutectic microstructure exhibiting Te-nanodomains and Sb-precipitates. A maximum $ZT \approx 1.4$ was attained at 500 K, which is amongst the highest reported values at higher temperature for *p*-type bulk nanostructured BST materials (Fig. 6). The attained higher *ZT* resembles the ones processed by top-down approaches (such as ball milling[5, 11, 12] and melt-spinning[14, 15]) and therefore exhibits considerable promise for fabricating commercial TE devices at low cost by thermo-chemical synthesis followed by spark plasma sintering.

Acknowledgement

We thank the members of the Nanochemistry Research Group (http://nanochemgroup.org) at INL for insightful discussions and support. This work was supported by Portuguese national funding agency for science, research, and technology (FCT) under the UT-BORN-PT project (UTAP-EXPL/CTE/0050/2017). B.A.K. acknowledges funding of this work by the Robert A. Welch Foundation (grant no. F-1464). The authors acknowledge the Texas Advanced Computing Center (TACC) at The University of Texas at Austin for providing HPC resources that have contributed to the research results reported within this paper. URL: http://www.tacc.utexas.edu.

Conflict of Interest: There is no conflict of interest to declare.

Data availability statement: The data that support the findings of this study are available upon request from the authors.

FIGURES

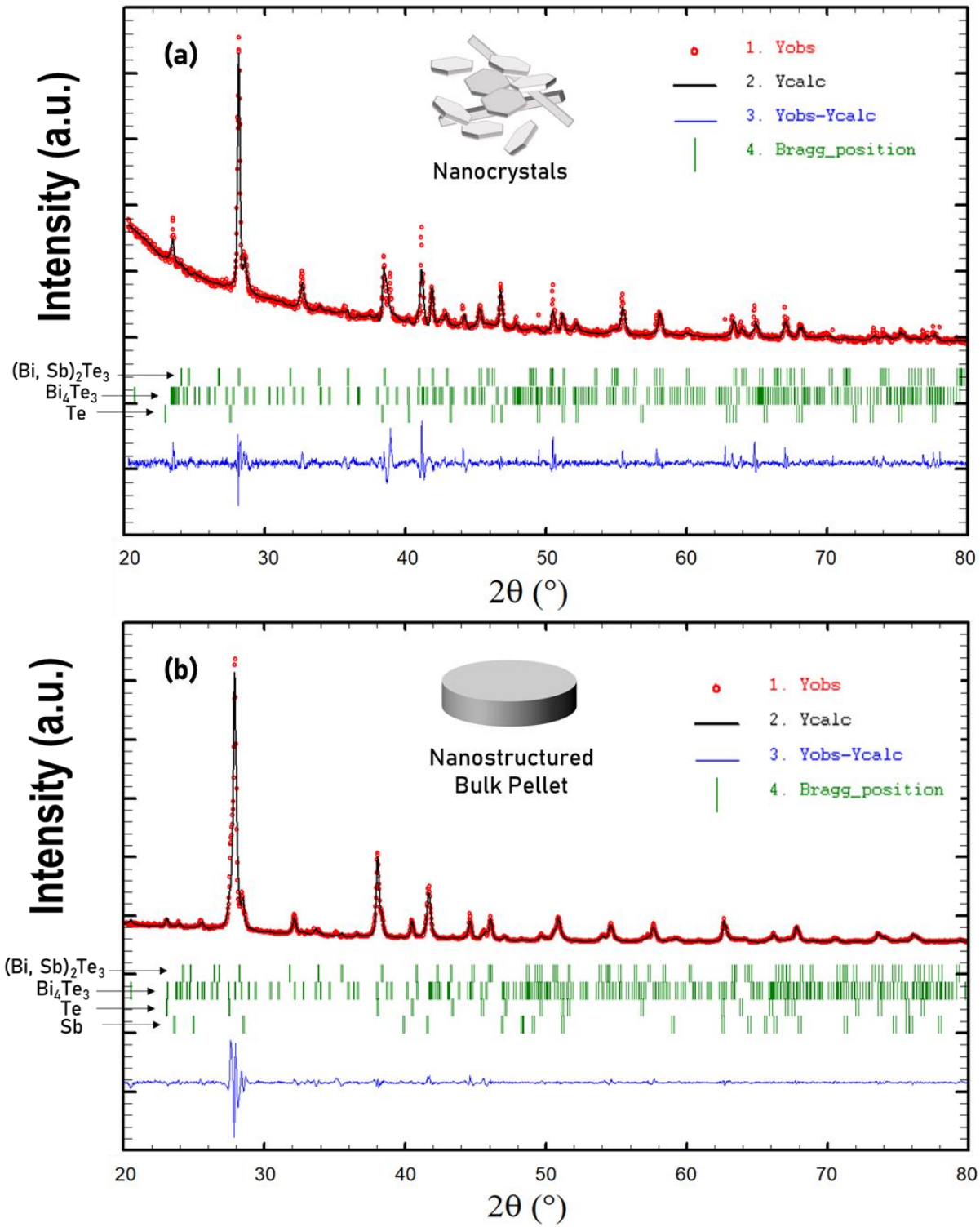

Figure 1: *Rietveld refinement of experimental powder X-ray diffraction patterns for colloidally-synthesized Bi–Sb–Te nanoparticles (a) and BST bulk nanocomposite prepared by the SPS consolidation of the Bi–Sb–Te nanoparticles (b).*

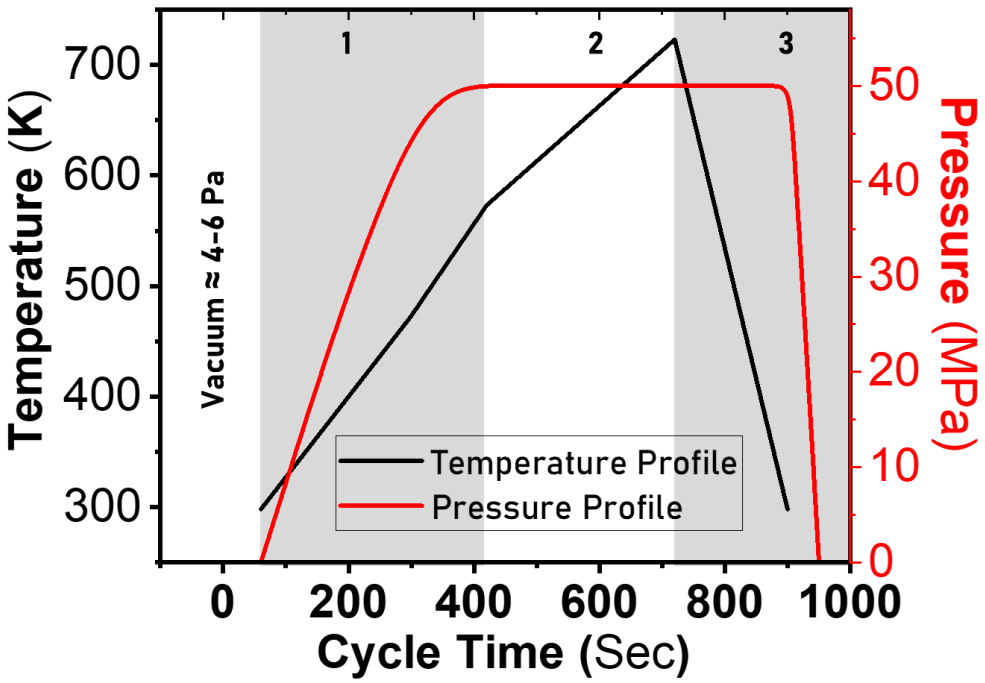

Figure 2. *Spark plasma sintering profile*

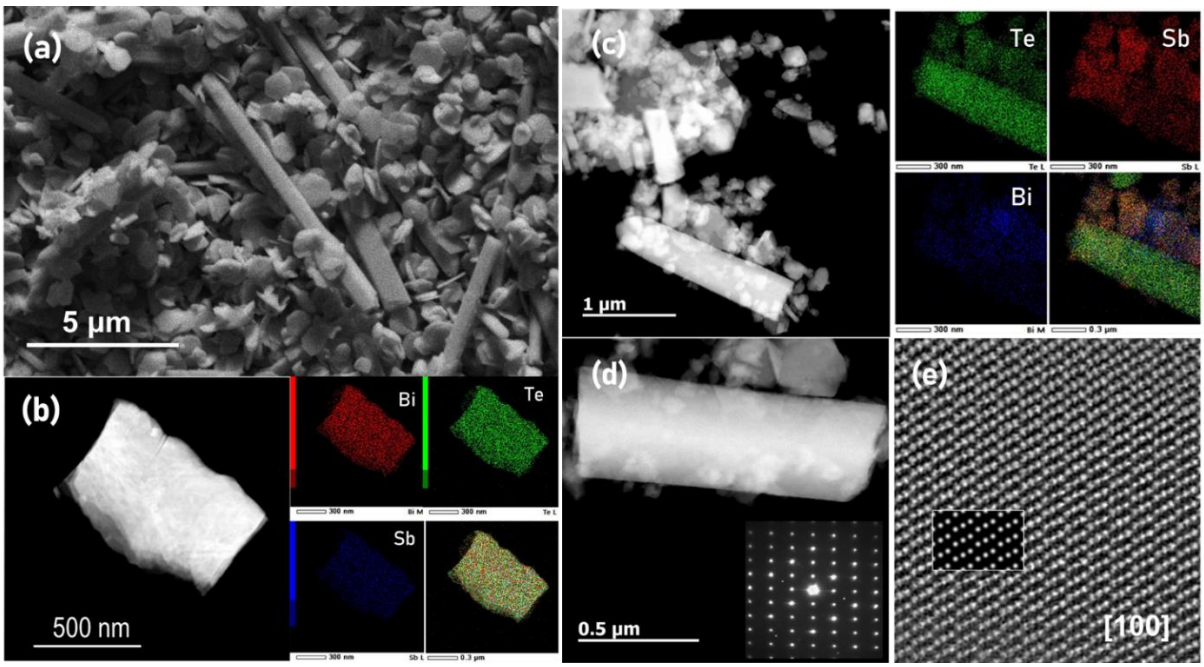

Figure 3: *Microstructural characterization of Bi-Sb-Te nanoparticles: (a) SEM image; HAADF–STEM image of the nanoparticles with (b) plate morphology and (c) rod shape morphology along with corresponding EDX elemental mapping of Bi, Sb, Te and overlaid color image (d) HAADF–STEM image of Te nanorod shown at higher magnification along with its corresponding SAED pattern shown in inset, together with the respective high-*resolution image along [100] zone axis *(e).*

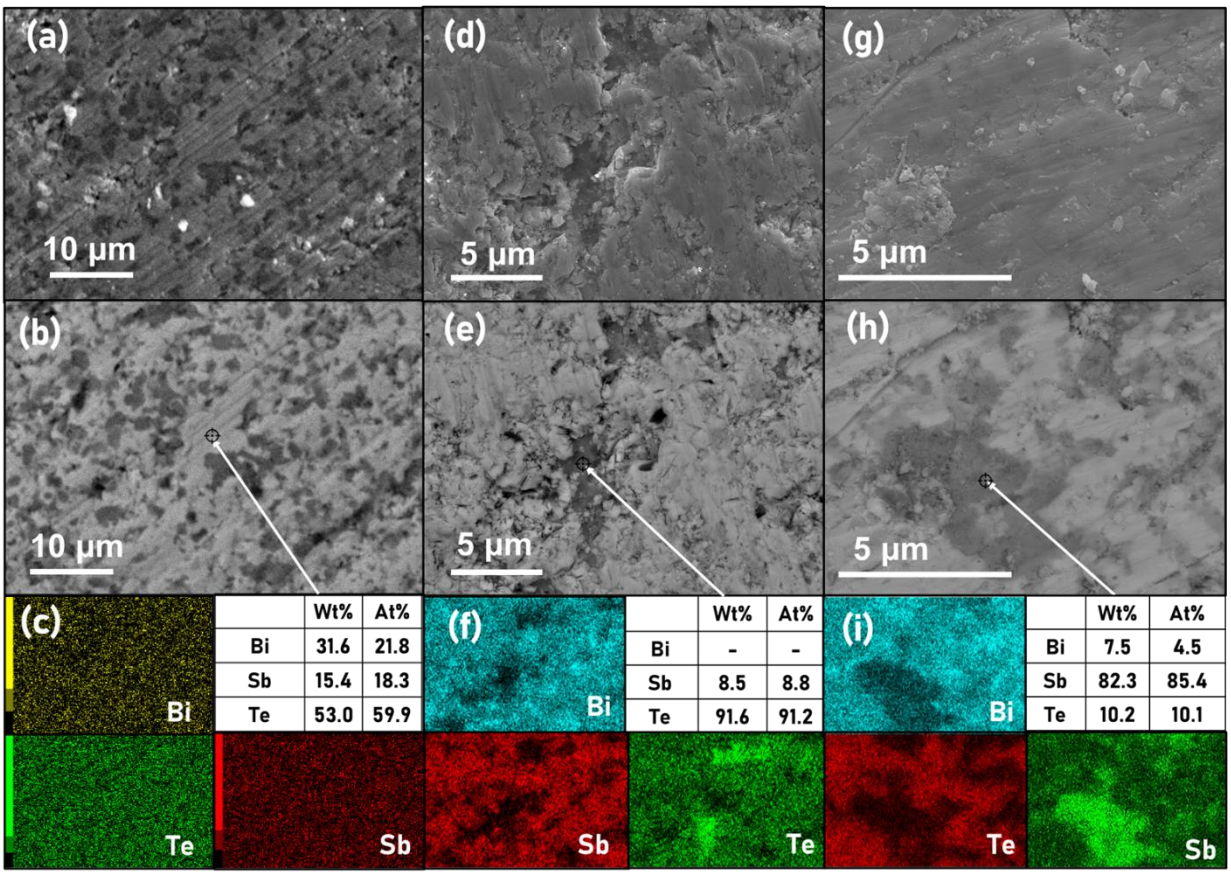

Figure 4: *Microstructural characterization of Bi-Sb-Te nanocomposite. At lower magnification well distributed darker regions within brighter appearing matrix displayed by (a) SE image and (b) BSE image along with corresponding (c) elemental mapping and EDS analysis of matrix; The darker region at higher magnification shown by (d) SE image and (e) BSE image along with its (f) elemental mapping and EDS analysis indicating Te rich region corresponding Te nanorods; The evidence of in-situ antimony precipitation revealed by (g) SE image and (h) BSE image along with its (i) elemental mapping and EDS analysis representing dark regions corresponding to in-situ Sb precipitates.*

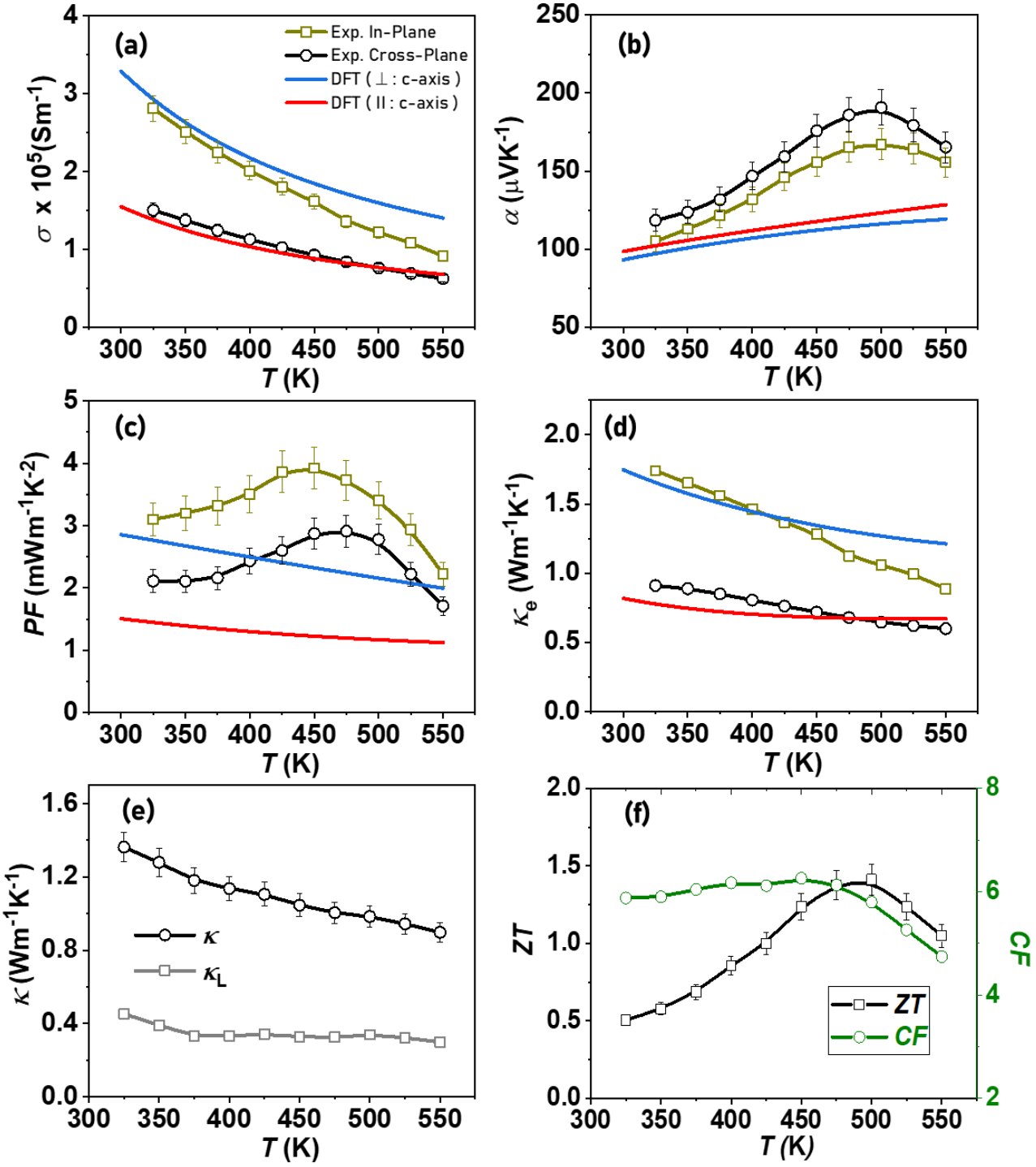

Figure 5: *Temperature-dependent transport properties of synthesized Bi-Sb-Te bulk nanocomposite, BST (a) electrical conductivity, (b) Seebeck coefficient, (c) power factor, (d) electronic thermal conductivity, (e) total and lattice thermal conductivity and (f) Thermoelectric figure-of-merit (ZT) & Compatibility Factor (CF).*

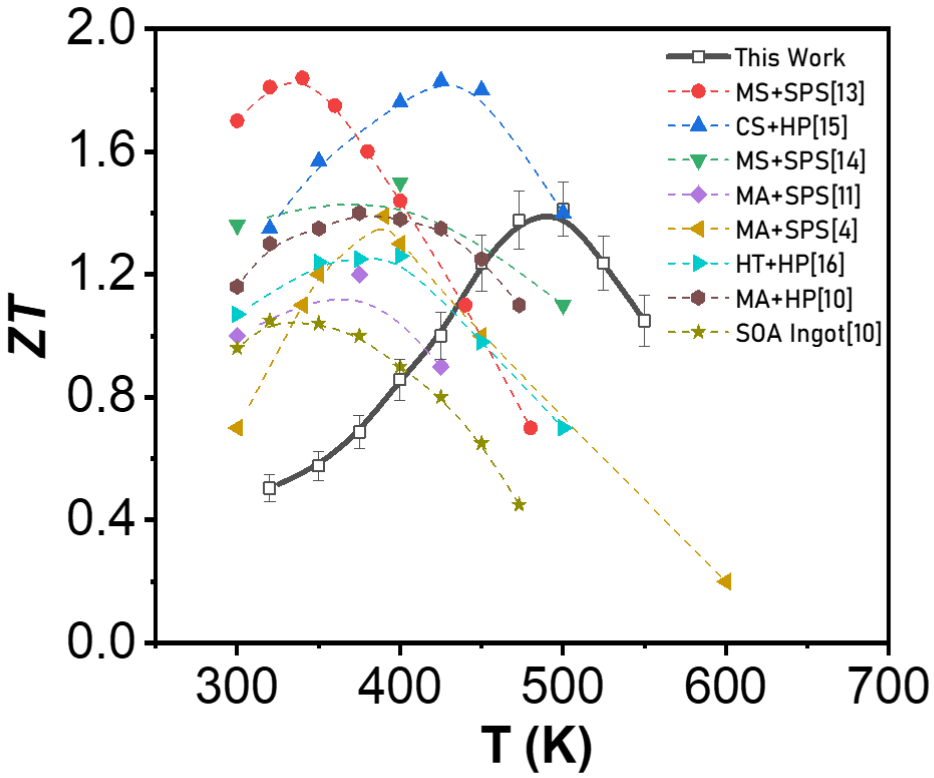

SOA: State-of-Art ; CS: Chemical Synthesis; MA: Mechanical Alloying; MS: Melt Spinning; HT: Hydrothermal; HP: Hot Pressing; SPS: Spark Plasma Sintering

Figure 6: *ZT comparison with state-of-the-art of p-type* $(Bi,Sb)_2Te_3$ *nanostructured bulk alloys.*

References

1. Snyder, G.; Toberer, E., Complex thermoelectric materials. *Nature Materials* **2008,** *7* (2), 105-114.
2. DiSalvo, F. J., Thermoelectric cooling and power generation. *Science* **1999,** *285* (5428), 703-706.
3. Jouhara, H.; Khordehgah, N.; Almahmoud, S.; Delpech, B.; Chauhan, A.; Tassou, S. A. J. T. S.; Progress, E., Waste heat recovery technologies and applications. **2018,** *6*, 268-289.
4. Goldsmid, H. J., Bismuth telluride and its alloys as materials for thermoelectric generation. *Materials* **2014,** *7* (4), 2577-2592.
5. Li, H.; Jing, H.; Han, Y.; Xu, Y.; Lu, G.-Q.; Xu, L., Microstructure and transport properties of copper-doped p-type BiSbTe alloy prepared by mechanical alloying and subsequent spark plasma sintering. *Journal of alloys and compounds* **2013,** *576*, 369-374.
6. Cui, J.; Xue, H.; Xiu, W.; Yang, W.; Xu, X., Thermoelectric properties of Cu-doped p-type pseudo-binary CuxBi0. 5Sb1. 5− xTe3 (x= 0.05–0.4) alloys prepared by spark plasma sintering. *Scripta materialia* **2006,** *55* (4), 371-374.
7. Wei, Z.; Li, Z.; Luo, P.; Zhang, J.; Luo, J., Simultaneously increased carrier concentration and mobility in p-type Bi0. 5Sb1. 5Te3 throng Cd doping. *Journal of Alloys and Compounds* **2020**, 154625.
8. Lee, J.; Park, S.; Kim, B.; Oh, M.; Cho, S.; Min, B.; Lee, H.; Kim, M., Control of thermoelectric properties through the addition of Ag in the Bi 0.5 Sb 1.5 Te 3 alloy. *Electronic Materials Letters* **2010,** *6* (4), 201-207.
9. Cui, J.; Xu, X., Transport properties of quaternary Ag–Bi–Sb–Te alloys prepared by pressureless sintering. *Materials Letters* **2005,** *59* (26), 3205-3208.
10. Kim, K.; Kim, G.; Lee, H.; Lee, K. H.; Lee, W., Band engineering and tuning thermoelectric transport properties of p-type Bi0. 52Sb1. 48Te3 by Pb doping for low-temperature power generation. *Scripta Materialia* **2018,** *145*, 41-44.
11. Poudel, B.; Hao, Q.; Ma, Y.; Lan, Y.; Minnich, A.; Yu, B.; Yan, X.; Wang, D.; Muto, A.; Vashaee, D., High-thermoelectric performance of nanostructured bismuth antimony telluride bulk alloys. *Science* **2008,** *320* (5876), 634-638.
12. Bulat, L.; Drabkin, I.; Karatayev, V.; Osvenskii, V.; Parkhomenko, Y. N.; Lavrentev, M.; Sorokin, A.; Pshenai-Severin, D.; Blank, V.; Pivovarov, G., Structure and transport properties of bulk nanothermoelectrics based on Bi x Sb 2− x Te 3 fabricated by SPS method. *Journal of electronic materials* **2013,** *42* (7), 2110-2113.
13. Pan, Y.; Aydemir, U.; Grovogui, J. A.; Witting, I. T.; Hanus, R.; Xu, Y.; Wu, J.; Wu, C. F.; Sun, F. H.; Zhuang, H. L., Melt-Centrifuged (Bi, Sb) 2Te3: Engineering Microstructure toward High Thermoelectric Efficiency. *Advanced Materials* **2018,** *30* (34), 1802016.
14. Kim, S. I.; Lee, K. H.; Mun, H. A.; Kim, H. S.; Hwang, S. W.; Roh, J. W.; Yang, D. J.; Shin, W. H.; Li, X. S.; Lee, Y. H., Dense dislocation arrays embedded in grain boundaries for high-performance bulk thermoelectrics. *Science* **2015,** *348* (6230), 109-114.
15. Xie, W.; Wang, S.; Zhu, S.; He, J.; Tang, X.; Zhang, Q.; Tritt, T. M., High performance Bi 2 Te 3 nanocomposites prepared by single-element-melt-spinning spark-plasma sintering. *Journal of Materials Science* **2013,** *48* (7), 2745-2760.
16. Liu, Y.; Zhang, Y.; Ortega, S.; Ibáñez, M.; Lim, K. H.; Grau-Carbonell, A.; Martí-Sánchez, S.; Ng, K. M.; Arbiol, J.; Kovalenko, M. V., Crystallographically Textured Nanomaterials Produced from the Liquid Phase Sintering of Bi x Sb2–x Te3 Nanocrystal Building Blocks. *Nano letters* **2018,** *18* (4), 2557-2563.

17. Chen, Z.; Xu, G.; Chen, S.; Zhang, J.; Wang, M., Hydrothermal synthesized nanostructure Bi–Sb–Te thermoelectric materials. *Journal of alloys and compounds* **2014,** *588*, 384-387.
18. Pakdel, A.; Guo, Q.; Nicolosi, V.; Mori, T. J. J. o. M. C. A., Enhanced thermoelectric performance of Bi–Sb–Te/Sb 2 O 3 nanocomposites by energy filtering effect. **2018,** *6* (43), 21341-21349.
19. Li, J.; Tan, Q.; Li, J. F.; Liu, D. W.; Li, F.; Li, Z. Y.; Zou, M.; Wang, K. J. A. F. M., BiSbTe-based nanocomposites with high ZT: the effect of SiC nanodispersion on thermoelectric properties. **2013,** *23* (35), 4317-4323.
20. Madavali, B.; Lee, C. H.; Kim, H. S.; Lee, K. H.; Hong, S. J. J. I. J. o. A. C. T., Investigation of microstructure and thermoelectric properties of p-type BiSbTe/ZnO composites. **2018,** *15* (1), 125-131.
21. Li, Y.; Dou, Y.; Qin, X.; Zhang, J.; Xin, H.; Li, D.; Song, C.; Zou, T.; Liu, Y.; Li, C. J. R. A., Enhanced thermoelectric figure of merit in p-type β-Zn 4 Sb 3/Bi 0.4 Sb 1.6 Te 3 nanocomposites. **2016,** *6* (15), 12243-12248.
22. Jiang, Z.; Ming, H.; Qin, X.; Feng, D.; Zhang, J.; Song, C.; Li, D.; Xin, H.; Li, J.; He, J. J. A. A. M.; Interfaces, Achieving High Thermoelectric Performance in p-Type BST/PbSe Nanocomposites through the Scattering Engineering Strategy. **2020,** *12* (41), 46181-46189.
23. Madavali, B.; Kim, H.-S.; Lee, K.-H.; Hong, S.-J. J. I., Enhanced Seebeck coefficient by energy filtering in Bi-Sb-Te based composites with dispersed Y2O3 nanoparticles. **2017,** *82*, 68-75.
24. Dou, Y.; Qin, X.; Li, D.; Li, L.; Zou, T.; Wang, Q. J. J. o. A. P., Enhanced thermopower and thermoelectric performance through energy filtering of carriers in (Bi2Te3) 0.2 (Sb2Te3) 0.8 bulk alloy embedded with amorphous SiO2 nanoparticles. **2013,** *114* (4), 044906.
25. Bergman, D. J.; Levy, O., Thermoelectric properties of a composite medium. *Journal of Applied Physics* **1991,** *70* (11), 6821-6833.
26. Chauhan, N. S.; Lebedev, O. I.; Kovnir, K.; Pyrlin, S. V.; Marques, L. S.; Ramos, M. M.; Korgel, B. A.; Kolen'ko, Y. V. J. N. A., Scalable colloidal synthesis of Bi 2 Te 2.7 Se 0.3 plate-like particles give access to a high-performing n-type thermoelectric material for low temperature application. **2020,** *2* (12), 5699-5709.
27. Sousa, V.; Gonçalves, B. F.; Franco, M.; Ziouani, Y.; González-Ballesteros, N.; Fátima Cerqueira, M.; Yannello, V.; Kovnir, K.; Lebedev, O. I.; Kolen'ko, Y. V., Superstructural Ordering in Hexagonal CuInSe2 Nanoparticles. *Chemistry of Materials* **2018,** *31* (1), 260-267.
28. Gonçalves, B. F.; LaGrow, A. P.; Pyrlin, S.; Owens-Baird, B.; Botelho, G.; Marques, L. S.; Ramos, M.; Kovnir, K.; Lanceros-Mendez, S.; Kolen'ko, Y. V. J. N., Large-Scale Synthesis of Semiconducting Cu (In, Ga) Se2 Nanoparticles for Screen Printing Application. **2021,** *11* (5), 1148.
29. Chen, Y.-H.; Liao, C.-N. J. A. P. L., Transport properties of electrically sintered bismuth antimony telluride with antimony nanoprecipitation. **2017,** *111* (14), 143901.
30. Witting, I. T.; Chasapis, T. C.; Ricci, F.; Peters, M.; Heinz, N. A.; Hautier, G.; Snyder, G. J. J. A. E. M., The thermoelectric properties of bismuth telluride. **2019,** *5* (6), 1800904.
31. Shi, E.; Cui, S.; Kempf, N.; Xing, Q.; Chasapis, T.; Zhu, H.; Li, Z.; Bahk, J.-H.; Snyder, G. J.; Zhang, Y. J. N. R., Origin of inhomogeneity in spark plasma sintered bismuth antimony telluride thermoelectric nanocomposites. **2019**, 1-8.
32. Liu, Y.; Zhang, Y.; Ortega, S.; Ibáñez, M.; Lim, K. H.; Grau-Carbonell, A.; Martí-Sánchez, S.; Ng, K. M.; Arbiol, J.; Kovalenko, M. V. J. N. l., Crystallographically

Textured Nanomaterials Produced from the Liquid Phase Sintering of Bi x Sb2–x Te3 Nanocrystal Building Blocks. **2018,** *18* (4), 2557-2563.
33. Liu, Y.; Zhang, Y.; Lim, K. H.; Ibáñez, M.; Ortega, S.; Li, M.; David, J.; Martí-Sánchez, S.; Ng, K. M.; Arbiol, J. J. A. n., High Thermoelectric Performance in Crystallographically Textured n-Type Bi2Te3–x Se x Produced from Asymmetric Colloidal Nanocrystals. **2018,** *12* (7), 7174-7184.
34. Lan, Y.; Poudel, B.; Ma, Y.; Wang, D.; Dresselhaus, M. S.; Chen, G.; Ren, Z. J. N. l., Structure study of bulk nanograined thermoelectric bismuth antimony telluride. **2009,** *9* (4), 1419-1422.
35. Kim, H.-S.; Gibbs, Z. M.; Tang, Y.; Wang, H.; Snyder, G. J., Characterization of Lorenz number with Seebeck coefficient measurement. *APL materials* **2015,** *3* (4), 041506.
36. Snyder, G. J.; Ursell, T. S., Thermoelectric efficiency and compatibility. *Physical review letters* **2003,** *91* (14), 148301.
37. Snyder, G. J.; Caillat, T., Using the compatibility factor to design high efficiency segmented thermoelectric generators. *MRS Online Proceedings Library Archive* **2003,** *793*.
38. Scherrer, H.; Martin-Lopez, R.; Lenoir, B.; Dauscher, A.; Scherrer, S. In *Thermoelectric materials of p and n type from the (Bi, Sb, Te) phase diagram*, Proceedings ICT2001. 20 International Conference on Thermoelectrics (Cat. No. 01TH8589), IEEE: 2001; pp 13-17.
39. Lošťák, P.; Drašar, Č.; Bachan, D.; Beneš, L.; Krejčová, A. J. R. e.; science, d. i. s. i. p.; technology, p., Defects in Bi2Te3− x Se x single crystals. **2010,** *165* (3), 211-215.
40. Horak, J.; Navratil, J.; Starý, Z. J. J. o. P.; Solids, C. o., Lattice point defects and free-carrier concentration in Bi2+ xTe3 and Bi2+ xSe3 crystals. **1992,** *53* (8), 1067-1072.
41. Liu, W. S.; Zhang, Q.; Lan, Y.; Chen, S.; Yan, X.; Zhang, Q.; Wang, H.; Wang, D.; Chen, G.; Ren, Z. J. A. E. M., Thermoelectric property studies on Cu-doped n-type CuxBi2Te2. 7Se0. 3 nanocomposites. **2011,** *1* (4), 577-587.
42. Zhang, Q.; Fang, T.; Liu, F.; Li, A.; Wu, Y.; Zhu, T.; Zhao, X. J. C. A. A. J., Tuning Optimum Temperature Range of Bi2Te3-Based Thermoelectric Materials by Defect Engineering. **2020,** *15* (18), 2775-2792.
43. Duan, X.; Jiang, Y. J. A. s. s., Annealing effects on the structural and electrical transport properties of n-type Bi2Te2. 7Se0. 3 thin films deposited by flash evaporation. **2010,** *256* (24), 7365-7370.
44. Kim, S. J.; Choi, H.; Kim, Y.; We, J. H.; Shin, J. S.; Lee, H. E.; Oh, M.-W.; Lee, K. J.; Cho, B. J. J. N. E., Post ionized defect engineering of the screen-printed Bi2Te2. 7Se0. 3 thick film for high performance flexible thermoelectric generator. **2017,** *31*, 258-263.
45. Wang, Q.; Yang, L.; Zhou, S.; Ye, X.; Wang, Z.; Zhu, W.; McCluskey, M. D.; Gu, Y. J. T. j. o. p. c. l., Phase-defined Van der Waals Schottky junctions with significantly enhanced thermoelectric properties. **2017,** *8* (13), 2887-2894.
46. Gibbs, Z. M.; Kim, H.-S.; Wang, H.; Snyder, G. J. J. A. P. L., Band gap estimation from temperature dependent Seebeck measurement—deviations from the 2e| S| maxTmax relation. **2015,** *106* (2), 022112.
47. Hu, L.-P.; Zhu, T.-J.; Wang, Y.-G.; Xie, H.-H.; Xu, Z.-J.; Zhao, X.-B. J. N. A. M., Shifting up the optimum figure of merit of p-type bismuth telluride-based thermoelectric materials for power generation by suppressing intrinsic conduction. **2014,** *6* (2), e88-e88.